Intrinsic local symmetry breaking in nominally cubic paraelectric $BaTiO_3$

Xin-Gang Zhao,[1] Oleksandr I. Malyi,[1] Simon J. L. Billinge,[2] and Alex Zunger[1,*]
[1]*Renewable and Sustainable Energy Institute, University of Colorado, Boulder, Colorado 80309, USA*
[2]*Department of Applied Physics and Applied Mathematics, Fu Foundation School of Engineering and Applied Sciences, Columbia University, New York, New York 10027, USA*

(Received 9 June 2021; revised 23 March 2022; accepted 25 March 2022; published 10 June 2022)

Whereas at low-temperatures ferroelectrics have a well understood ordered spatial dipole arrangement, the fate of these dipole configurations in the higher temperature paraelectric (PE) phase remains poorly understood. Using density functional theory (DFT), we find that, unlike the case in nonpolar ABO_3, perovskites such as cubic $BaZrO_3$ that do not lower their energy by any form of positional symmetry breaking, the origin of distribution of the B-site off-centering in cubic PE such as $BaTiO_3$ is an intrinsic, energy lowering due to symmetry breaking. Minimizing the internal energy E_0 of a constrained cubic phase represented by a large enough supercell to accommodate symmetry breaking already reveals the presence of a distribution of local displacements (i.e., a polymorphous network) that (i) *locally* mimics the symmetries of the low temperature phases, while (ii) being the precursors of what finite temperature density functional theory (DFT) molecular dynamics (MD) finds as thermal motifs when equilibrating the free energy $E_0 - TS$. Analyzing the DFT-derived configurations of the PE cubic supercell by projecting its displacements onto irreducible representations reveals that it is best described as a temperature-dependent superposition of numerous modes, including ferroelectric ($\Gamma_4{}^-$) and antiferroelectric ($M_2{}^-$ and $X_5{}^+$), rather than a single mode, (e.g., $X_5{}^+$) representing a well-defined long-range ordered configuration. This suggests that the electronic and dielectric properties of such PE phases are best calculated from a polymorphous distribution of interrelated local motifs in large supercells rather than from either purely disordered or long-range ordered models. In this respect, PE phases share a common feature with paramagnetic (PM) and paraelastic (PEL) perovskite phases whose central feature is a polymorphous distribution of local motifs—dipole moments in PE, magnetic moments in PM, and ordinary octahedral distortion modes in PEL—all computable by DFT supercells and useable in calculating electronic and magnetic properties of paraphases.

DOI: 10.1103/PhysRevB.105.224108

Oxide perovskites ABO_3, typified by $BaTiO_3$ (BTO), have local dipoles $\{\mu^{(i)}{}_{\text{local}}\}$, formed by polar atomic displacements off high symmetry positions i. At low temperatures, these can organize into ferroelectric (FE) long-range-ordered (LRO) structures. Above the Curie temperature $T_C \sim 401$ K, BTO transforms into a cubic paraelectric (PE) phase, [1] whose microscopic configuration is poorly understood. Crystallographically, this high-temperature PE structure, as well as that of the experimentally reported ∼90 other perovskite oxide [2,3] and scores of halide perovskites [4,5], are classified as Pm-$3m$ space group symmetry with a single formula unit per cell. A central question in this field [6–16] regards the nature of the spatial configurations of the local $\{\mu^{(i)}{}_{\text{local}}\}$ dipoles in such PE phases. Suppose the Pm-$3m$ paraelectric phase, consisting of a single, undeformed octahedral motif as its repeat unit (the monomorphous configuration), is taken literally rather than as a "virtual crystal" average over configurations. In this case, the PE phase will not only have vanishing global dipole moment $\mu_{\text{global}} \sim 0$, but also vanishing local dipoles on each site, $\{\mu^{(i)}{}_{\text{local}} = 0\}$ [a "nonelectric" configuration; Fig. 1(a) inset]. Experimentally, in contrast, the pioneering 1968 diffuse scattering x-ray diffraction measurements of Comes *et al.* [9] on the PE phase were interpreted as being due to the presence of nonzero local dipoles $\{\mu^{(i)}{}_{\text{local}}\}$ that persist locally in the high-temperature cubic phase of BTO. Other measurements also seem to indicate the off-centering of the Ti ions not only in the low-temperature FE phases but also in the PE phase. This includes nuclear magnetic resonance (NMR) [10], atomic pair distribution function (PDF) analysis of neutron powder diffraction data [11–13], x-ray absorption fine structure (EXAFS) [14], as well as the observation of birefringence [17], second harmonic generation (SHG), [18] and piezoelectricity in cubic oxide paraelectrics [19,20]. The SHG and piezoelectricity effects, however, are forbidden in the centrosymmetric nominal cubic phase, suggesting that locally the symmetry in PE BTO is noncentrosymmetric. Although some sightings of such "forbidden symmetries" appear to involve *extrinsic* factors (such as defects [21] or growth-induced nonideal microstructures [22]), there are cases, most prominently BTO [23], where *intrinsic symmetry breaking* appears to be at play. Other experiments, the most notably inelastic neutron scattering [24,25], suggest that the local dipoles appear only on cooling through the FE phase transition. The resulting controversy has held the perovskite community in fascination for over 50 years. This dilemma can be posed in the following way: Is the PE condition of $\mu_{\text{global}} \sim 0$ realized by having (a) $\{\mu^{(i)}{}_{\text{local}} = 0\}$ [symmetry unbroken, absence

---

[*] Corresponding author: Alex.Zunger@colorado.edu

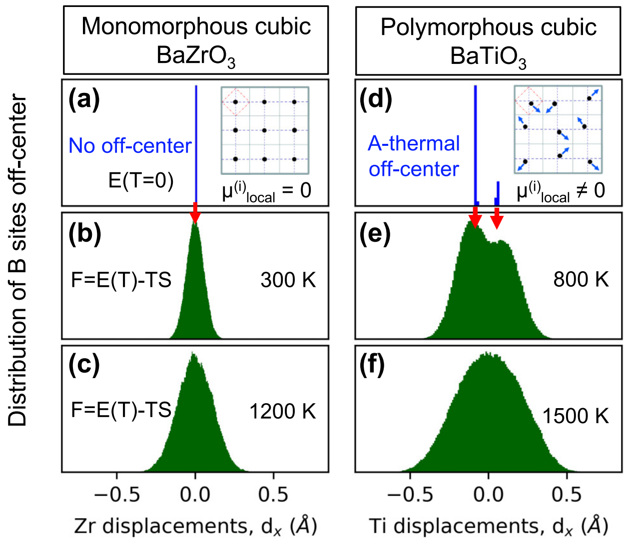

FIG. 1. (XC = PBE) Distribution of projected B-site displacements d_x in ABO_3 with respect to the center of mass of an octahedron is shown for the cubic BaZrO$_3$ in (a)–(c), and the intrinsically symmetry breaking cubic BaTiO$_3$ in (d)–(e). Inserts in (a) and (d) are the schematic illustrations of the B atomic displacements in models of cubic monomorphous and polymorphous structures. The displacements were taken from ∼20000 snapshots on equilibrated MD trajectories with NPT ensemble ($N = 64$ f.u./cell; $P = 1$ atm; $\Delta t = 1$ fs). The asymmetric distribution as shown in (e) was discussed in Appendix C.

of local dipoles, as illustrated in Fig. 1(a) inset] or (b) via distribution of mutually compensating nonzero local dipoles $\{\mu^{(i)}_{\text{local}} \neq 0\}$ [Fig. 1(d) inset]. What makes the resolution of this conundrum important is that the choice between (a) and (b) strongly affects the nature of predictions of calculations of spectroscopic and transport properties. For example, the use of the monomorphous view (a) ubiquitous in standard databases [26–29] as input to calculations often leads to a significant underestimation of band gaps [30–33]. An analogous dilemma exists in interpreting the nature of the distribution of local moments in paramagnetic (PM) phases of magnetic oxide perovskites, where one assumes the view of a minimal Pm-3m unit cell with a single formula unit, common in electronic structure calculations of PM phases, leads to well-known contradictions with data.

On the other hand, possibility (b) has been generally interpreted by attributing local dipoles in the PE phase to *thermal fluctuations,* where atoms are oscillating thermally around their Wyckoff positions and time averaging to a zero polarization. However, such thermal effects do not account for the intrinsic nature of the polarization implied by the macroscopic experiments [34]. Indeed, there is also a possible contribution from modes driven by intrinsic effects (such as the nature of the chemical bonding in such phases) even before thermal motion sets in. Such intrinsic, athermal symmetry breaking is known in inorganic compounds, such as degeneracy removal exemplified by the Jahn-Teller distortions of d orbital impurities in insulators [35], or by the lone-pair s orbitals of Sn, Pb, or Bi centers in inorganic compounds [36], or via sterically induced octahedral rotations and tilting in perovskites [37], all understood as athermal energy lowering symmetry breaking that can exist prior to thermal agitation.

The present work offers a different view on the *origin and properties* of the microscopic structure of PE phases, using as an example the classic cubic PE BaTiO$_3$. We start with first-principles minimization of the *internal energy* E_0 followed by a finite temperature MD simulation of its *free energy* $F = E_0 - TS$. The computational details used for internal energy minimization, as well as the description of the different exchange-correlation (XC) functionals and the finite-temperature MD simulation, are explained in Appendixes A and B.

We find that the displacement pattern in the finite temperature cubic PE phase evident in MD simulations follows a blueprint encoded already by the athermal symmetry breaking that emerges from a constrained minimization of the internal energy E_0 for a cubic phase. As a reference point, we recall that conventional "monomorphous" compounds such as Si, GaAs, or BaZrO$_3$ [the latter shown in Figs. 1(a)–1(c)] are not stabilized by intrinsic symmetry breaking and thus give the same calculated result per atom if a small unit cell of a given symmetry is used, or a larger supercell replica. However, in the PE cubic phase of BaTiO$_3$, the resulting "polymorphous network" exhibits a pattern of intrinsic, athermal off-center displacements [shown by the blue lines in Fig. 1(d) and the leading red arrows]. As temperature rises [Fig. 1(e)], the underlying polymorphous pattern in BTO is initially retained at intermediate temperatures before it is overwhelmed by strong thermal motions at higher temperatures [Fig. 1(f)]. The latter displacement pattern is now centered symmetrically at the zero-displaced position, akin to a behavior characteristic of conventional monomorphous compounds [Figs. 1(a)–1(c)] at *all temperatures.*

Compared with using monomorphous Pm-3m configuration, the displacement patterns show better agreement with the measured PDF [11–13]. The distributed intrinsic symmetry breaking is enabled only if one allows a larger than minimal high symmetry unit cell which has the geometric flexibility to break symmetry—should the internal energy E_0 be lowered.

The emergence of such a polymorphous network consisting of an energy lowering distribution of local environments is a fundamentally important result with broad implications. It is an example where allowing the structure to have symmetry lowering distortions, even whilst respecting the global, "average" cubic symmetry, that density functional theory (DFT) can find *intrinsic symmetry broken structures that lower the energy of the system.* They are intrinsic in the sense that the distortions are not a result of extrinsic imperfections such as defects or doping. We believe that not all, but many, structures will do this, especially ones with high susceptibilities to various applied forces such as the ferroelectrics discussed here. It not only explains poorly understood experimental observations in BTO but more broadly gives us a recipe for finding new functional materials by using DFT to search for previously unknown polymorphous network materials. In this respect, PE phases share a common feature with paramagnetic (PM) and paraelastic (PEL) perovskite phases whose central feature is a polymorphous distribution of local motifs—dipole moments in PE, magnetic moments in PM, and ordinary octahedral distortion modes in PEL—all computable by DFT supercells and useable in calculating electronic and magnetic properties of paraphases.

The present approach to the microscopic understanding of paraphases allows us to learn a great deal about symmetry breaking. For example, upon projecting the displacement field on the irreducible representation, we find the *hidden polar FE-like mode* Γ_4^- with given $4 \times 4 \times 4$ supercell, forbidden in the nominal cubic structure but consistent with the experimentally observed SHG [18] and piezoelectricity [19,20] that are disallowed in centrosymmetric (e.g., *Pm*-3*m*) phases. It is significant that the MD study using the classic force field (lacking explicit electronic degrees of freedom) demonstrates [16] at temperature above T_c a symmetric displacement field, producing zero net polarization. Furthermore, in contrast to commonly used approximations [38] that describe the PE phase as an *averaged* high-symmetry cubic structure that is *nonelectric* (vanishing global polarization because all local dipoles are also zero), we deduce that neither averaged monomorphous cubic *Pm*-3*m* (used in thousands of previous studies) nor a long-range ordered cubic antiferroelectric (AFE) phase with single type AFE mode [39,40] commonly invoked is the universally physical model to describe the structural properties and electronic structure of PE phases.

Theoretical approach. To understand the possible significance of symmetry breaking within the PE phase and whether it emerges from intrinsic or thermal effects, we use a polymorphous DFT (polyDFT) approach [41,42]. In brief, it (i) does not restrict the *local* symmetry of the PE phase to that of a monomorphous *Pm*-3*m* structure having a single local motif, (ii) does not use a long-range-ordered dipole model for the PE phase that has fixed Wyckoff positions in a given cubic space group [39,40]. Nor does it use the Special Quasirandom Structures (SQS) method that is appropriate for studying paramagnetic disorder [45] rather than (correlated) positional atomic displacements investigated here (Fig. 3 below). (iii) Instead, it explores both intrinsic (via minimization of the internal energy E_0) and dynamic (via thermal evolution of the free energy $F = E_0 - TS$ in first-principles molecular dynamics). To allow unimpeded local symmetry breaking while respecting the *global* cubic symmetry, we constrain the lattice vectors to the macroscopically observed cubic shape $a = b = c$ but allow internal symmetry breaking if it lowers the energy (another choice, not used here, is to constrain both the cubic cell shape and the internal atomic positions to cubic symmetry [39,40]). The type of superposition of ordered configurations that emerge from our minimization procedure will be apparent from the projection of the results on a basis set of representations analysis (Fig. 3). We use enlarged unit cells [here, 64 formula units (f.u.), i.e., 320 atoms; the results are rather robust against further cell enlargement]. Table I (Appendix B) demonstrates the rather weak dependence of the result on the initial configuration and on the random atomic nudges used to initialize the minimization.

The results are analyzed to study the correlation between different displacements by projecting the displacement field on irreducible representations as done in Duyker *et al.* [43]. We do so via DFT that retains explicit electronic and lattice degrees of freedom. Whereas using a first-principles description limits supercell size and simulation time, the appearance of an active irreducible representation mode Γ_4^- shown in Fig. 3 at all temperatures clearly predicts correlated displacements. However, it does not capture the few nm-scale correlated displacements that have been reported experimentally near T_c [9].

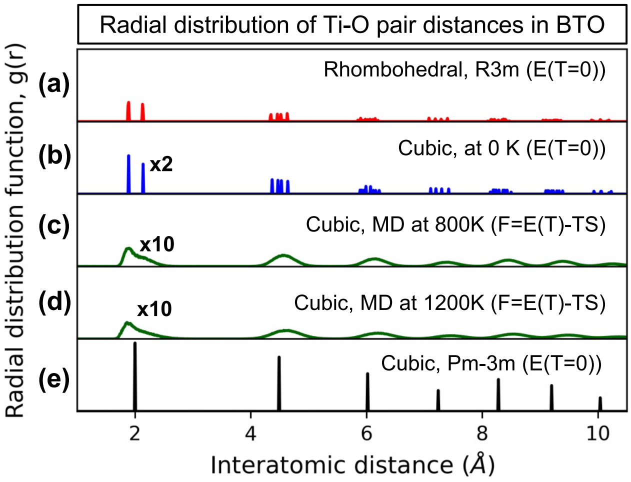

FIG. 2. (a)–(e) Ti-O RPDF before and after temperature set in (XC = PBE). Here, (a) is the RPDF for the intrinsic rhombohedral phase (1 f.u./cell), (b) is for the intrinsic polymorphous network, and (c) and (d) are from 100 snapshots equilibrium trajectories of MD simulation in the *NPT* ensemble at 1 atm, 800 and 1200 K with interval 0.1 ps. Finally, (e) shows RPDF in nominal cubic phase (1 f.u./cell).

The distribution of Ti-O atomic pairs in paraelectric phase (Fig. 2). We consider the partial radial distribution function (PRDF), $g(r)_{ab}$, between species a and species b, defined as

$$g(r)_{ab} = \frac{1}{N_a} \sum_{i=1}^{N_a} \frac{\sum_{j=1}^{N_b} \langle \delta(|r_{ij} - r|) \rangle}{4\pi r^2 dr}, \qquad (1)$$

where $N_{\rm a}$ and $N_{\rm b}$ refer to the total number of atoms for each species and r_{ij} is the length of the vector from atom i to atom j. The PRDF of Ti-O pairs in the ground FE rhombohedral structure is shown in Fig. 2(a) and compared with the results of the polymorphous PE cubic network with intrinsic distortion [blue lines Fig. 2(b)] and with snapshots at 800 and 1200 K of the MD profile [Figs. 2(c) and 2(d)]. Significantly, we find, in the polymorphous cubic PE phase, a splitting of the nearest-neighbor Ti-O peak [Fig. 2(b)]. This splitting is due to the emergence of the set of local Ti off-center displacements [Fig. 2(b)]. No constraint is placed on the directions of symmetry lowering displacements in the DFT calculations, which are guided simply by lowering the internal energy. However, we note that the displacements occur predominantly along {111} directions, which is consistent with the ground state rhombohedral structure and the experimental observations of local structural probes [9,11,14], resulting in the formation of three short (1.88 Å) and three long (2.13 Å) Ti-O bonds. A remnant of the nearest-neighbor Ti-O bond splitting is also observed in PRDFs obtained from our finite temperature MD calculations at temperatures of 800 K [green line in Fig. 2(c)], presenting a large asymmetry peak. Interestingly, the polymorphous cubic PE phase also has local structural motifs that are not present in either the nominal cubic monomorphous approximant [Fig. 2(e)] or the

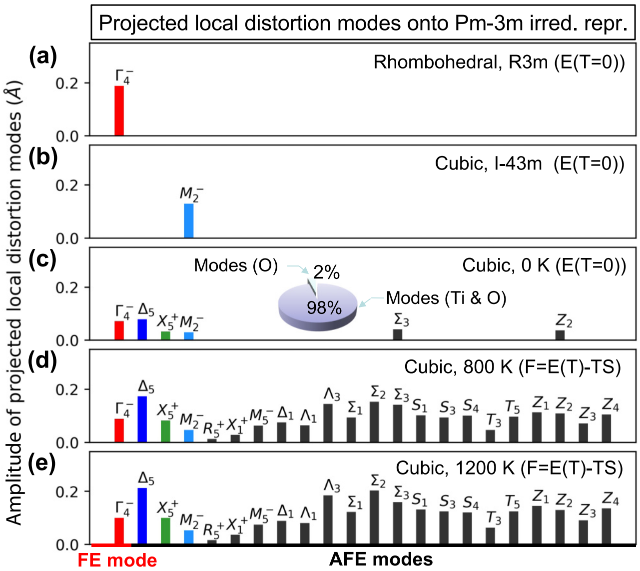

FIG. 3. (XC = PBE) Projected distortion modes related to Ti and oxygen intrinsic and thermal displacements onto parent undistorted cubic (Pm-$3m$) irreducible representations of (a) ground state rhombohedral structure (1 f.u./cell), (b) *ordered* AFE cubic phase (I-$43m$, 8 f.u./cell), (c) supercell structure with the distributed intrinsic distortions, and (d),(e) snapshots (64 f.u./cell) on equilibrated MD trajectory. Inset to (c) shows the indicated modes projected onto atomic displacements. The heights of bars in (c)–(e) refer to the averaged amplitude of each mode for each of the 10, 100, and 100 configurations, respectively. The ten configurations in (c) are obtained from ten independent runs starting from the renudged supercell structures (see Table I). Each of 100 configurations in (d) and (e) are extracted with interval 0.1 ps from the equilibrated MD trajectory with *NPT* ensemble at 800 and 1200 K, pressure 1 atm, and time step 1 fs. Γ_4^- is FE-like Ti displacement, whereas the rest of the mode are AFE-like relative Ti displacements.

low-temperature FE phase [Fig. 2(a)]. However, the PRDF of other pairs in the polymorphous network (Appendix D) shows relatively small broadening in the range 1–8 Å but no apparent asymmetry of the first-nearest peaks. This might be because of the Goldschmidt tolerance factor [43,44] $t_{\mathrm{eff}} = \frac{R_A+R_O}{\sqrt{2}(R_B+R_O)}$ of cubic BTO (1.06) is slightly larger than 1, so octahedral tilting/rotation or A-site displacements are small.

Local symmetry breaking driven by the internal energy: The characteristic of a polymorphous [41,42,45] structure of a material is that the total energy per atom in a supercell constrained to have the same shape as the macroscopically observed "average structure" is seen to initially decrease as the supercell size increases before saturating at a certain supercell size. We find that *cubic* BTO is polymorphous (average energy reduction -24 ± 2 meV/f.u. [Perdew-Burke-Ernzerhof (PBE)] relative to the monomorphous approximation), with predominantly Ti off-center displacements [Fig. 2(b)]. Not all materials are polymorphous, as shown in Fig. 1(a): the non-paraelectric $BaZrO_3$ has only thermal motion. Indeed, we find that this is the case for BTO in its ground state rhombohedral structure ($R3m$, space group 160), where there is no symmetry breaking induced intrinsic energy reduction on increasing the cell size.

The decomposition of intrinsic and dynamic distortion fields in terms of irreducible representations of the cubic Pm-3m symmetry (Fig. 3). The polyDFT calculations show a local symmetry breaking in cubic BTO, although this calculation step excludes any effects due to the finite temperature. This points to an intrinsic energetic driving force for forming local distortions under the set of constraints given. It is interesting to inquire what is the origin of the intrinsic symmetry-breaking mode symmetries in the PE phase. We find that these symmetries are inherited from the low-temperature long-range ordered FE phase as well as theoretically predicted long-range ordered cubic AFE phase with zero net total dipole [39,40], albeit without the long-range dipolar order, as indicated by their irreducible representation modes in Figs. 3(a) and 3(b) (computational details are provided in Appendix A). Specifically, the low-temperature FE rhombohedral phase is a condensation of just one of these modes—the one associated with the Γ_4^- irrep [Fig. 3(a)], whereas the predicted AFE phase is associated with M_2^- irrep. The intrinsic polymorphous model of the PE phase shows that the projected Γ_4^- irrep mode is still one of the most prominent modes [Fig. 3(c)] at $T = 0$, resulting in a Ti off-centering that is almost as large (0.09 Å) as in the rhombohedral phase (0.20 Å). However, the Γ_4^- is not the only significant mode that is populated in the polymorphous network. Five additional modes—X_5^+, Σ_3, M_2^-, Z_2, and Δ_5—all with AFE patterns, have significant amplitudes. These modes originate from relative Ti displacements along opposite {100} directions in different TiO_2 layers. For example, for X_5^+, the AFE-like Ti displacements occur in adjacent TiO_2 layers, whereas for Δ_5, the AFE-like Ti displacements occur in three TiO_2 layers, in which the Ti displacements in the middle TiO_2 layer are not displaced. These additional X_5^+, Σ_3, M_2^-, Z_2, and Δ_5 modes have distortion magnitudes in the range 0.04–0.10 Å. Importantly, they robustly appear in all independently restarted polymorphous calculations (Table I in Appendix B), suggesting they are a robust part of the polymorphous state and not due to incomplete sampling. Since Δ_5, Σ_3, M_2^-, Z_2, and X_5^+ are absent in the globally rhombohedral phase, presumably, they play a role in relaxing the local distortion.

Thermal effects on paraelectric modes and Ti distributions. To capture thermal effects, we use MD simulations starting from the intrinsic polymorphous results. The MD runs result in atomic configurations that can also be decomposed onto the basis of the distortional modes of irreps as was done for the polyDFT relaxed structures in Fig. 3(c). As expected, as the temperature is raised, many additional modes become significantly populated. For example, the mode populations averaged over 100 snapshots (within 10-ps time scale) in MD simulation at 800 and 1200 K are shown in Figs. 3(d) and 3(e), indicating that the Γ_4^-, M_2^-, and X_5^+ symmetry modes remain active even at 1200 K, i.e., well into the PE phase, despite the fact that new modes join in the symmetry breaking and the relative magnitude of each mode is temperature dependent. Further, the projected Ti displacements at 800 and 1200 K (see Figs. 1 and 6) also indicate that the off-center distortion, though the prominently off-center contribution at 800 K seems to be gradually overcome as temperature increases to 1200 K, is a close center-flat-like distribution. The center-flat-like distribution has been observed based on the

MD simulation with a force field and interpreted as mixed character of "order-disorder" and "displacive" [15,16] near T_c. Indeed, Paściak *et al.* [16] found that the on-center population of Ti atoms is shallow at $T_c + 100$ K. Therefore, the off-center vector might be changed due to thermal effect, but will never be a dominated population at zero as in a cubic polymorphous network at $T = 0$ K.

The net polarity in the paraelectric phase and its dependence on temperature. The projections described above give important insights into the nature of the collective distortion modes of the system, but it gives incomplete information about the polarizability of the material. To quantify this, we need to consider the size of the local electric dipoles $\{\mu^{(i)}{}_{\text{local}}\}$, which are proportional to the displacements of Ti atoms away from the center of their local O_6 octahedral hosts. These Ti displacements can be represented with respect to the mass center of the octahedron in polymorphous structures and MD snapshots. The projections of Ti displacements along the ⟨100⟩ direction are shown in Figs. 1(e) and 1(f) for a 64 f.u. supercell for different temperatures, showing the presence of Ti off-centering. This effect has been ascribed previously to the thermal effect [16], but it emerges here from the static calculation, suggesting the origin is electronic symmetry breaking associated with this energy lowering. The ensuing intrinsic net polarization is $\sim 0.15 \pm 0.01$ Å (XC = PBE) oriented close to the ⟨111⟩ direction before the temperature sets in. Further, by averaging all dipoles $|\sum_1^N \vec{d}|$ over a ∼40-ps period on the equilibrium MD trajectories, we find that the global dipole is diminished with temperature: $\mu_{\text{global}} = 0.02$ and 0.01 Å at 800 and 1200 K, respectively. This nonzero global polarization is due to the $\Gamma_4{}^-$ mode (Fig. 3) with a local FE-like pattern in a $4 \times 4 \times 4$ supercell, which is different from predicted long-range ordered cubic $BaTiO_3$ with zero net dipole [39,40]. In our calculation, the net global polarization around T_c is not zero, in agreement with the measured polarization of single crystal BTO above T_c [46,47]. This nonzero polarization might contribute to anomalous observations, such as Raman splitting [48], SHG [18], piezoelectricity [19,20], those are seen in PE cubic BTO. As shown in Figs. 1(e) and 1(f), Ti displacements change off-center to on-center vibration as temperature increases from 800 to 1200 K (also see Appendix C). The off-center Ti displacements are observed at 1200 K. We note that the temperature at which such displacements can be observed might be overestimated because of the overestimated lattice expansion by PBE functional. This finding is different from the general understanding (i.e., above T_c, the PE phase is described by the displacive model [47] as a single parabolic well, lacking static displacements) of the PE phase at finite temperatures.

We conclude that in addition to the usual thermally driven disorder in conventional compounds such as $BaZrO_3$, other compounds such as PE $BaTiO_3$ manifest an *intrinsic* athermal precursor to symmetry breaking in the form of a ("polymorphous") distribution of energy-lowering local motifs. These can survive at finite temperatures in the PE phase, providing a physical understanding of the microscopic structures and their anomalous phenomenon in these kinds of PE materials.

We acknowledge fruitful discussions with E. K. H. Salje and A. Bussmann-Holder on paraelectrics, Z. Wang on the long-range-order model of AFE, and L. D. Yuan for assistance in calculating polymorphous structures with different initial nudges shown in Table I (Appendix B). The work in Zunger's group was supported by the U.S. National Science Foundation through Grant No. DMREF-1921949. The work in Billinge's group was supported by the US National Science Foundation through grant DMR-1922234. The calculations were done using the Extreme Science and Engineering Discovery Environment (XSEDE), which was supported by National Science Foundation Grant No. ACI-1548562.

APPENDIX A: COMPUTATIONAL DETAILS

All the structural optimizations were carried out using the density functional theory (DFT) within ionic pseudopotential and plane-wave basis set with the Perdew-Burke-Ernzerhof (PBE) [49] exchange-correlation (XC) functional, as implemented in the VASP code [50,51]. The valence electron configurations for creation of the ionic pseudopotentials were Ba($5s^25p^66s^2$), Ti($3d^34s^1$), O($2s^22p^4$), and Zr($4s^24p^64d^35s^1$), respectively. The energy threshold was set to 1×10^{-6}eV/cell, and the force on each atom was converged to <0.01 eV/Å. All the *ab initio* calculations management and data postprocessing were done using an open resource named the JAMIP program [52].

Internal energy minimization. A $12 \times 12 \times 12$ k-point was used to get 1 f.u./cell structure lattice constants by keeping global Pm-$3m$ symmetry. The $4 \times 4 \times 4$ supercells with initial nudges (0.01 Å with random direction) were roughly optimized using a Gamma-only k-point grid within frozen out shape and lattice constants of the supercell, then the force on each atom was carefully relaxed with $3 \times 3 \times 3$ k-point grid. To get the accurate differences of total internal energy between undistorted structure (called nominal cubic) and optimized supercell (called polymorphous), we calculated the internal energies of all the structures with the same cell size ($4 \times 4 \times 4$ supercells) and k grid ($3 \times 3 \times 3$ k-point) using the PBE [49] (for comparison, XC = SCAN [53] that gives more accurate of total energy is also considered) functional as shown in Table I in Appendix B.

Ab initio molecular dynamic simulations (AIMD) and prediction of Curie temperature. To study the local symmetry breaking at finite temperatures, we carried the AIMD using a $4 \times 4 \times 4$ supercell (64 f.u./cell) with a polymorphous nature, PBE functional, Gamma-only k grid, and NPT ensemble (Langevin thermostat [54]) at 500, 600, 700, 800, 1200, and 1500 K, respectively (the measured Curie temperature and melting point for cubic $BaTiO_3$ is $T_c = 401$ [11] and 1893 K, [55] respectively). The friction coefficients using a Langevin thermostat are set to 1 ps^{-1} for Ba, Ti, Zr, and O atomic degree of freedom and 100 ps^{-1} for lattice degree of freedom. The time step is set to 1 fs.

The ideal Pm-$3m$ $BaTiO_3$ has a lattice constant $c/a = 1$. The experimentally measured c/a value of the tetragonal phase lattice constant is ∼1.010 [56], and the value extracted from the MD simulation and DFT calculation is ∼1.026 [15]. Here, the Curie temperature from the tetragonal to cubic phase is estimated by checking the ratio of lattice constant

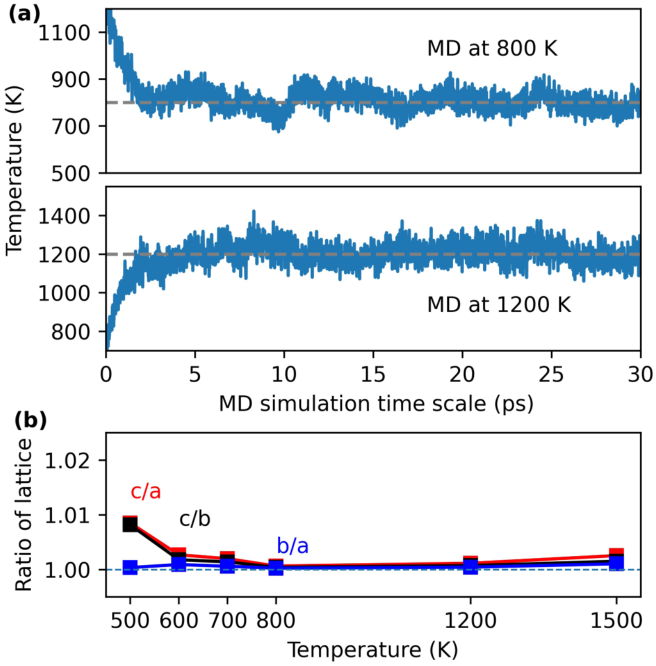

FIG. 4. (a) Temperature fluctuation as a function of MD simulation time for 800 and 1200 K. (b) The ratio of lattice constants of BTO as temperature increases. The lattice constants *a*, *b*, and *c* at each temperature are the averaged values of lattice constants for all the snapshots within 10-ps MD simulations trajectory when temperatures reach the initially set constant value.

c/a at different temperatures without considering the atomic positions.

As shown in Fig. 4(a), the temperature reaches the constant value after ~10 ps at 800 and 1200 K starting from the DFT polymorphous kernel configurations (4 × 4 × 4 supercell). Therefore, the statistical analysis (e.g., Ti displacements, lattice constants) of AIMD simulations at finite temperatures shown in all figures is based on the snapshots on the equilibrated trajectories after 10 ps. As shown in Fig. 4(b), the AIMD simulation reveals that there is a relatively sharp change of the c/a value from 1.004 at 600 K to 1.020 at 500 K. Therefore, we propose that the Curie temperature from the tetragonal to cubic phase for $BaTiO_3$ is roughly between ~500 and ~600 K based on our input parameters with *NPT* ensemble at 1 atm in a 4 × 4 × 4 supercell.

Projected Ti displacements. In $BaTiO_3$, we define the off-center displacement for each Ti atom as a vector from the coordinates of the virtual mass center C_i^0 of the host octahedron O_6 to the coordinates of the actual Ti position C_i in the Cartesian coordinate, expressed as $\vec{d} = C_i - C_i^0$, where $i = 1$–64 is the index of Ti in the 64 f.u./cell. The vector is projected to the ⟨100⟩, ⟨010⟩, and ⟨001⟩ directions of 1 f.u./cell *Pm*-3*m* cubic $BaTiO_3$, which is defined as d_x, d_y, and d_z, respectively. The detailed discussion on projected Ti displacements is addressed in Appendix C.

Projected irreducible representation modes on Pm-3m symmetry. This analysis involves describing a low symmetry structure as arising from the parent high symmetrized structure with one or more static structural distortions [57].

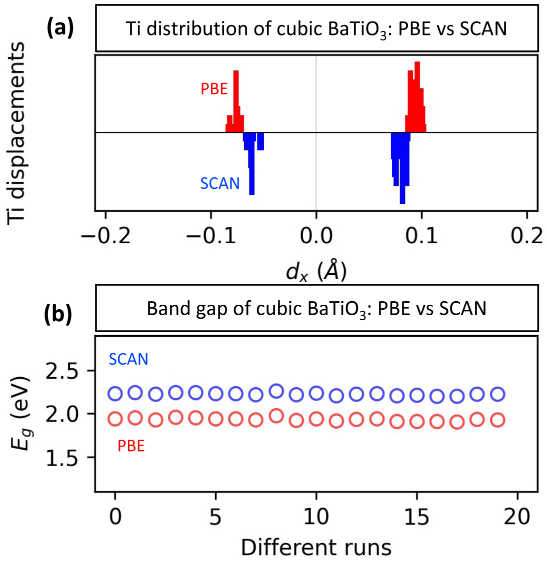

FIG. 5. Comparison of Ti displacements in polymorphous structure ID no. 20 and band gaps of 20 cubic polymorphous structures using PBE and SCAN functionals.

The undistorted parent structure has zero amplitudes for all the potential structural distortion modes described by the irreducible representation of the high-symmetry structure. In low symmetry structures, structural distortion modes with nonzero amplitudes are called active modes. This analysis can isolate the distortions in a low symmetry structure with complex local distortions and provide the contribution of active modes by comparing their amplitudes. The projected distortions to the adapted symmetry mode in the nominal cubic structure were obtained using ISOTROPY software [58]. The distortion modes with amplitude >0.01 Å are ordered from modes with the largest amplitude to the smallest amplitude in Table I (Appendix B).

APPENDIX B: COMPARISON OF ENERGY MINIMIZATION AND BY USING DIFFERENT CORRELATION FUNCTIONAL

As shown in Fig. 5 and Table I, we find that the intrinsic symmetry breaking occurs in all runs, resulting in total energy lowering with respect to undistorted cubic *Pm*-3*m* structure is −21 to −26 meV/f.u. (PBE) and −12 to −16 meV/f.u. (SCAN). Using different XC functionals does not qualitatively change the physical observation, i.e., symmetry breaking resulting in internal energy lowering and nonzero net Ti off-center displacements. Quantitively, the values of net off-center displacements, total energy lowering as well as band gap, and distribution of Ti atoms are shifted along the same direction when using different XC.

APPENDIX C: PROJECTED TI DISPLACEMENTS IN CUBIC $BaTiO_3$ BEFORE AND AFTER TEMPERATURE SETS IN

Figure 6 shows the distribution of the projected Ti displacements along with d_x, d_y, and d_z in ten (ID nos. 01–10 in Table I of Appendix B) structures obtained by minimizing

TABLE I. Properties of cubic $BaTiO_3$ with polymorphous nature from 20 runs. The net dipole is defined as the absolute value of the sum of displaced Ti vectors with respect to the mass center of the octahedron. Internal energy lowering of cubic $BaTiO_3$ is the enthalpy difference between the polymorphous configuration and the undistorted *Pm*-3*m* configuration. Configurations ID nos. 01–10 are obtained starting from *Pm*-3*m* configuration with an initial random nudge (0.01 Å) on each atom. Configurations ID nos. 11–20 structures are obtained starting from no. 04 by re-adding random nudge (0.01 Å) on each atom. All the configurations are obtained within the fixed lattice constants equal to optimized *Pm*-3*m* $BaTiO_3$. The irreducible representation modes with amplitude >0.01 Å for each configuration and two long-range ordered cubic $BaTiO_3$ are also listed.

	Net dipole (Å)		Energy lowering (meV/f.u.)		
ID	PBE	SCAN	PBE	SCAN	Irrep. modes (> 0.01 Å)
01	0.15	0.08	−24	−14	
02	0.15	0.05	−21	−12	
03	0.15	0.06	−23	−13	
04	0.16	0.06	−26	−15	
05	0.15	0.01	−22	−12	
06	0.15	0.03	−23	−13	
07	0.15	0.02	−23	−13	
08	0.15	0.04	−22	−12	$\Gamma_4{}^-$
09	0.15	0.07	−23	−13	Δ_5
10	0.15	0.03	−24	−14	$X_5{}^+$
11	0.15	0.06	−24	−15	$M_2{}^-$
12	0.16	0.08	−26	−16	Σ_3
13	0.15	0.06	−24	−14	Z_2
14	0.15	0.08	−25	−15	
15	0.15	0.08	−26	−16	
16	0.15	0.06	−24	−14	
17	0.15	0.07	−25	−15	
18	0.15	0.07	−24	−14	
19	0.16	0.07	−26	−16	
20	0.15	0.05	−23	−14	
21	0.00	0.00	*I*-43*m*, Refs. [39,40]		$M_2{}^-$
22	0.00	0.00	*P*−*a*3, Ref. [40]		$X_5{}^+$

internal energy E_0 and ∼20000 snapshots at different finite temperatures (XC = PBE).

Here, we use two quantities—amplitude of *off center*, defined as $d_{\max} \leftarrow \max[\sum_i^N \sum_j^{64} \delta(|d_{ij} - d_{\max}|)]$ and amplitude of *asymmetry* defined as $\langle d\rangle = \frac{\sum_i^N \sum_j^{64} d_{ij}}{64N}$, to quantitively evaluate the local Ti displacements.

We focus on two aspects here: (i) Symmetry breaking manifested by the off-center displacements in the PE phase being the central result, and (ii) the fact that the symmetry breaking is slightly asymmetric—a fact contributed in part most likely by the numerical aspect.

(i) As shown in Fig. 6, the *off-center* $d_{\max}$ along d_x, d_y, and d_z in cubic $BaTiO_3$ is ∼0.08 Å using the internal

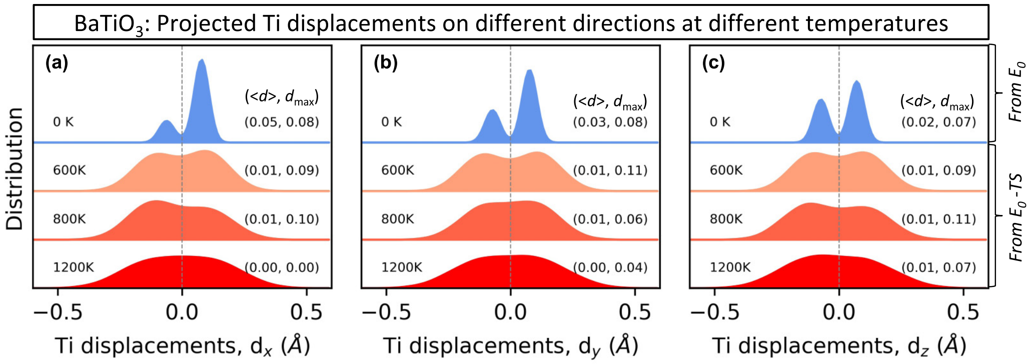

FIG. 6. (a)–(c) Distribution of the projected Ti displacements d_x, d_y, and d_z of configurations at different temperatures. The first row (in blue) is obtained by constrained minimization of the internal energy E_0 of a supercell with cubic lattice vectors but relaxed cell-internal atomic sites. Finite temperatures resulted (in red) are from molecular dynamics. All show symmetry breaking for $T < 800$ K, which is reduced at higher temperature to a flat featureless distribution; $N = \sim 20\,000$ snapshots are used for obtaining the Ti displacements at 600, 800, and 1200 K as well as ten configurations (i.e., ID nos. 01–10, see Table I in Appendix B) with polymorphous nature before temperature set in ($T = 0$). The values in the paratheses refer to amplitude (asymmetry, off center).

energy alone before temperature sets in, presenting two off-center peaks. The distribution of Ti displacements at 800 K mimics the polymorphous distribution seen in the supercell before the temperature sets in, having $d_{\max} = \sim 0.10$ Å. The two-peak distribution gradually transforms to a flat and structureless distribution as temperatures increase above the predicted Curie temperature, with a decrease of $d_{\max}$ from ~0.10 at 800 K to ~0.04 at 1200 K in the same time window (20 ps) and cell size (64 f.u./cell). The decrease of $d_{\max}$ at finite temperatures indicates that the thermal effects can suppress the off-center characteristic.

(ii) The *asymmetry of the two-peak symmetry breaking plot in* the distribution of projected Ti displacements in Fig. 6 is ~0.03 when the internal energy alone is used, whereas the asymmetry at 800 K is smaller (~0.01) and is close to zero at 1200 K within a 20-ps time window and 64-f.u. cell size. The amplitude of the *asymmetry* at 800 K is reduced (by <10%) but is not zero when considering from 20 to 60 ps, pointing out that the simulation time (or the cell size) might be contributing factors to this asymmetry.

APPENDIX D: PARTIAL RADIAL DISTRIBUTION FUNCTION (PRDF) IN CUBIC BaTiO$_3$

Figure 7 shows PRDFs of the Ba-Ba, Ba-Ti, Ti-Ti, Ba-O, and O-O pairs in the nominal cubic and in polymorphous cubic BaTiO$_3$ before and after the temperature set in. The positions of peaks along the nominal cubic, polymorphous structures are identical. However, the relative intensities of peaks in polymorphous structures at ~10 Å for Ba-Ba pairs, ~6.5 Å, and ~10 Å for Ti-Ti pairs, > ~5 Å for Ba-O pair, and > ~2.5 Å for O-O pairs are not in good agreement with the nominal cubic structure. Note that none of the pairs except Ti-O show significant asymmetry of the first peaks, indicating the existence of the locally off-center Ti.

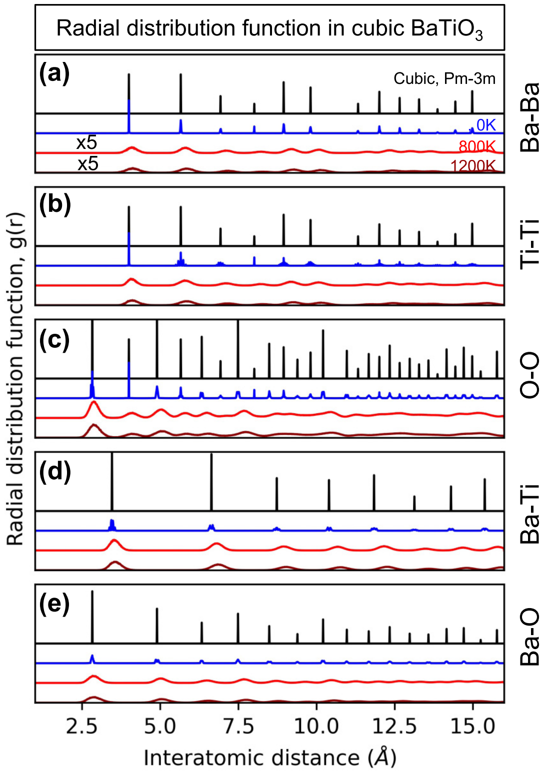

FIG. 7. (a)–(e) Comparison of pair distributions (Ba-Ba, Ti-Ti, O-O, Ba-Ti, and Ba-O) among nominal cubic (space group 221, black line), cubic BaTiO$_3$ with polymorphous nature (blue curve), and MD snapshots at 800 K (red curve) and 1200 K (dark red curve).

[1] M. B. Smith, K. Page, T. Siegrist, P. L. Redmond, E. C. Walter, R. Seshadri, L. E. Brus, and M. L. Steigerwald, Crystal structure and the paraelectric-to-ferroelectric phase transition of nanoscale BaTiO$_3$, J. Am. Chem. Soc. **130**, 6955 (2008).

[2] C. J. Bartel, C. Sutton, B. R. Goldsmith, R. Ouyang, C. B. Musgrave, L. M. Ghiringhelli, and M. Scheffler, New tolerance factor to predict the stability of perovskite oxides and halides, Sci. Adv. **5**, eaav0693 (2021).

[3] P. V. Balachandran, A. A. Emery, J. E. Gubernatis, T. Lookman, C. Wolverton, and A. Zunger, Predictions of New *AB*O$_3$ perovskite compounds by combining machine learning and density functional theory, Phys. Rev. Materials **2**, 043802 (2018).

[4] J. Wiktor, U. Rothlisberger, and A. Pasquarello, Predictive determination of band gaps of inorganic halide perovskites, J. Phys. Chem. Lett. **8**, 5507 (2017).

[5] Q. Sun and W.-J. Yin, Thermodynamic stability trend of cubic perovskites, J. Am. Chem. Soc. **139**, 14905 (2017).

[6] K. A. Müller and W. Berlinger, Microscopic probing of order-disorder versus displacive behavior in BaTiO$_3$ by Fe^{3+} EPR, Phys. Rev. B **34**, 6130 (1986).

[7] A. Bussmann-Holder, H. Beige, and G. Völkel, Precursor effects, broken local symmetry, and coexistence of order-disorder and displacive dynamics in perovskite ferroelectrics, Phys. Rev. B **79**, 184111 (2009).

[8] W. Zhong, D. Vanderbilt, and K. M. Rabe, Phase Transitions in BaTiO$_3$ from First Principles, Phys. Rev. Lett. **73**, 1861 (1994).

[9] R. Comes, M. Lambert, and A. Guinier, The chain structure of BaTiO$_3$ and KNbO$_3$, Solid State Commun. **6**, 715 (1968).

[10] R. Blinc and B. Žekš, Dynamics of order-disorder-type ferroelectrics and anti-ferroelectrics, Adv. Phys. **21**, 693 (1972).

[11] M. S. Senn, D. A. Keen, T. C. A. Lucas, J. A. Hriljac, and A. L. Goodwin, Emergence of Long-Range Order in BaTiO$_3$ from Local Symmetry-Breaking Distortions, Phys. Rev. Lett. **116**, 207602 (2016).

[12] G. H. Kwei, S. J. L. Billinge, S.-W. Cheong, and J. G. Saxton, Pair-Distribution functions of ferroelectric perovskites: direct observation of structural ground states, Ferroelectrics **164**, 57 (1995).

[13] K. Page, T. Proffen, M. Niederberger, and R. Seshadri, Probing local dipoles and ligand structure in BaTiO$_3$ nanoparticles, Chem. Mater. **22**, 4386 (2010).

[14] B. Ravel, E. A. Stern, R. I. Vedrinskii, and V. Kraizman, Local structure and the phase transitions of BaTiO$_3$, Ferroelectrics **206**, 407 (1998).

[15] Y. Qi, S. Liu, I. Grinberg, and A. M. Rappe, Atomistic description for temperature-driven phase transitions in BaTiO$_3$, Phys. Rev. B **94**, 134308 (2016).

[16] M. Paściak, T. R. Welberry, J. Kulda, S. Leoni, and J. Hlinka, Dynamic Displacement Disorder of Cubic $BaTiO_3$, Phys. Rev. Lett. **120**, 167601 (2018).

[17] J.-H. Ko, T. H. Kim, K. Roleder, D. Rytz, and S. Kojima, Precursor dynamics in the ferroelectric phase transition of barium titanate single crystals studied by brillouin light scattering, Phys. Rev. B **84**, 094123 (2011).

[18] A. M. Pugachev, V. I. Kovalevskii, N. V. Surovtsev, S. Kojima, S. A. Prosandeev, I. P. Raevski, and S. I. Raevskaya, Broken Local Symmetry in Paraelectric $BaTiO_3$ Proved by Second Harmonic Generation, Phys. Rev. Lett. **108**, 247601 (2012).

[19] E. K. H. Salje, X. Ding, and O. Aktas, Domain glass, Phys. Status Solidi B **251**, 2061 (2014).

[20] S. Hashemizadeh, A. Biancoli, and D. Damjanovic, Symmetry breaking in hexagonal and cubic polymorphs of $BaTiO_3$, J. Appl. Phys. **119**, 094105 (2016).

[21] O. Aktas, S. Crossley, M. A. Carpenter, and E. K. H. Salje, Polar correlations and defect-induced ferroelectricity in cryogenic $KTaO_3$, Phys. Rev. B **90**, 165309 (2014).

[22] E. K. H. Salje, M. A. Carpenter, G. F. Nataf, G. Picht, K. Webber, J. Weerasinghe, S. Lisenkov, and L. Bellaiche, Elastic excitations in $BaTiO_3$ single crystals and ceramics: Mobile domain boundaries and polar nanoregions observed by resonant ultrasonic spectroscopy, Phys. Rev. B **87**, 014106 (2013).

[23] M. Eremenko, V. Krayzman, A. Bosak, H. Y. Playford, K. W. Chapman, J. C. Woicik, B. Ravel, and I. Levin, Local atomic order and hierarchical polar nanoregions in a classical relaxor ferroelectric, Nat. Commun. **10**, 1 (2019).

[24] J. Harada, J. D. Axe, and G. Shirane, Neutron-scattering study of soft modes in cubic $BaTiO_3$, Phys. Rev. B **4**, 155 (1971).

[25] I. Tomeno, J. A. Fernandez-Baca, S. Chi, K. Oka, and Y. Tsunoda, Coexistence of soft modes and dynamic Ti disorder in cubic $BaTiO_3$ studied by inelastic neutron scattering, J. Phys. Soc. Jpn. **89**, 054601 (2020).

[26] A. Belsky, M. Hellenbrandt, V. L. Karen, and P. Luksch, New developments in the inorganic crystal structure database (ICSD): Accessibility in support of materials research and design, Acta Crystallogr., Sect. B: Struct. Sci., Cryst. Eng. Mater. **58**, 364 (2002).

[27] A. Jain, S. P. Ong, G. Hautier, W. Chen, W. D. Richards, S. Dacek, S. Cholia, D. Gunter, D. Skinner, G. Ceder, and K. A. Persson, Commentary: The materials project: A materials genome approach to accelerating materials innovation, APL Mater. **1**, 011002 (2013).

[28] S. Kirklin, J. E. Saal, B. Meredig, A. Thompson, J. W. Doak, M. Aykol, S. Rühl, and C. Wolverton, The open quantum materials database (OQMD): Assessing the accuracy of DFT formation energies, Npj Comput. Mater. **1**, 15010 (2015).

[29] S. Curtarolo, W. Setyawan, G. L. W. Hart, M. Jahnatek, R. V. Chepulskii, R. H. Taylor, S. Wang, J. Xue, K. Yang, O. Levy, M. J. Mehl, H. T. Stokes, D. O. Demchenko, and D. Morgan, AFLOW: An automatic framework for high-throughput materials discovery, Comput. Mater. Sci. **58**, 218 (2012).

[30] O. I. Malyi and A. Zunger, False metals, real insulators, and degenerate gapped metals, Appl. Phys. Rev. **7**, 041310 (2020).

[31] C. M. I. Okoye, Theoretical study of the electronic structure, chemical bonding and optical properties of $KNbO_3$ in the paraelectric cubic phase, J. Phys.: Condens. Matter **15**, 5945 (2003).

[32] S. Saha, T. P. Sinha, and A. Mookerjee, Electronic structure, chemical bonding, and optical properties of paraelectric $BaTiO_3$, Phys. Rev. B **62**, 8828 (2000).

[33] S. Cabuk, H. Akkus, and A. M. Mamedov, Electronic and optical properties of $KTaO_3$: *Ab Initio* calculation, Physica B **394**, 81 (2007).

[34] A. Bencan, E. Oveisi, S. Hashemizadeh, V. K. Veerapandiyan, T. Hoshina, T. Rojac, M. Deluca, G. Drazic, and D. Damjanovic, Atomic scale symmetry and polar nanoclusters in the paraelectric phase of ferroelectric materials, Nat. Commun. **12**, 1 (2021).

[35] A. Zunger, Electronic structure of 3d transition-atom impurities in semiconductors, in *Solid State Physics*, edited by H. Ehrenreich, and D. Turnbull, Vol. 39 (Academic, NewYork, 1986), pp. 275–464.

[36] A. F. Wells, *Structural Inorganic Chemistry* (Oxford University Press, Oxford, 2012).

[37] A. Mercy, J. Bieder, J. Íñiguez, and P. Ghosez, Structurally triggered metal-insulator transition in rare-earth nickelates, Nat. Commun. **8**, 1677 (2017).

[38] R. E. Cohen, Origin of ferroelectricity in perovskite oxides, Nature (London) **358**, 136 (1992).

[39] Q. Zhang, T. Cagin, and W. A. Goddard, The ferroelectric and cubic phases in $BaTiO_3$ ferroelectrics are also antiferroelectric, Proc. Natl Acad. Sci. USA **103**, 14695 (2006).

[40] M. Kotiuga, S. Halilov, B. Kozinsky, M. Fornari, N. Marzari, and G. Pizzi, A microscopic picture of paraelectric perovskites from structural prototypes, Phys. Rev. Research **4**, L012042 (2022).

[41] X.-G. Zhao, G. M. Dalpian, Z. Wang, and A. Zunger, Polymorphous nature of cubic halide perovskites, Phys. Rev. B **101**, 155137 (2020).

[42] X.-G. Zhao, Z. Wang, O. I. Malyi, and A. Zunger, Effect of static local distortions vs. dynamic motions on the stability and band gaps of cubic oxide and halide perovskites, Mater. Today **49**, 107 (2021).

[43] S. G. Duyker, J. A. Hill, C. J. Howard, and A. L. Goodwin, Guest-activated forbidden tilts in a molecular perovskite analogue, J. Am. Chem. Soc. **138**, 11121 (2016).

[44] V. M. Goldschmidt, Die gesetze der krystallochemie, Naturwissenschaften **14**, 477 (1926).

[45] G. Trimarchi, Z. Wang, and A. Zunger, Polymorphous band structure model of gapping in the antiferromagnetic and paramagnetic phases of the mott insulators MnO, FeO, CoO, and NiO, Phys. Rev. B **97**, 035107 (2018).

[46] X. Moya, E. Stern-Taulats, S. Crossley, D. González-Alonso, S. Kar-Narayan, A. Planes, L. Mañosa, and N. D. Mathur, Giant electrocaloric strength in single-crystal $BaTiO_3$, Adv. Mater. **25**, 1360 (2013).

[47] G. Burns and F. H. Dacol, Polarization in the cubic phase of $BaTiO_3$, Solid State Commun. **42**, 9 (1982).

[48] A. M. Quittet and M. Lambert, Temperature dependence of the raman cross section and light absorption in cubic $BaTiO_3$, Solid State Commun. **12**, 1053 (1973).

[49] J. P. Perdew, K. Burke, and M. Ernzerhof, Generalized Gradient Approximation Made Simple, Phys. Rev. Lett. **77**, 3865 (1996).

[50] G. Kresse and J. Furthmüller, Efficiency of *ab-initio* total energy calculations for metals and semiconductors

using a plane-wave basis set, Comput. Mater. Sci. **6**, 15 (1996).

[51] G. Kresse and J. Furthmüller, Efficient iterative schemes for ab initio total-energy calculations using a plane-wave basis set, Phys. Rev. B **54**, 11169 (1996).

[52] X.-G. Zhao, K. Zhou, B. Xing, R. Zhao, S. Luo, T. Li, Y. Sun, G. Na, J. Xie, X. Yang, X. Wang, X. Wang, X. He, J. Lv, Y. Fu, and L. Zhang, JAMIP: an artificial-intelligence aided data-driven infrastructure for computational materials informatics, Sci. Bull. **66**, 1973 (2021).

[53] J. Sun, A. Ruzsinszky, and J. P. Perdew, Strongly Constrained and Appropriately Normed Semilocal Density Functional, Phys. Rev. Lett. **115**, 036402 (2015).

[54] W. G. Hoover, A. J. C. Ladd, and B. Moran, High-Strain-Rate Plastic Flow Studied Via Nonequilibrium Molecular Dynamics, Phys. Rev. Lett. **48**, 1818 (1982).

[55] O. L. G. Alderman, C. J. Benmore, J. Neuefeind, A. Tamalonis, and R. Weber, Molten barium titanate: A high-pressure liquid silicate analogue, J. Phys.: Condens. Matter **31**, 20LT01 (2019).

[56] C. Moriyoshi, S. Hiramoto, H. Ohkubo, Y. Kuroiwa, H. Osawa, K. Sugimoto, S. Kimura, M. Takata, Y. Kitanaka, Y. Noguchi, and M. Miyayama, Synchrotron radiation study on time-resolved tetragonal lattice strain of $BaTiO_3$ under electric field, Jpn. J. Appl. Phys. **50**, 09NE05 (2011).

[57] P. V. Balachandran, N. A. Benedek, and J. M. Rondinelli, in *Symmetry-Adapted Distortion Modes as Descriptors for Materials Informatics, in Information Science for Materials Discovery and Design*, edited by T. Lookman, F. J. Alexander, and K. Rajan (Springer, Cham, 2016), pp. 213–222.

[58] B. J. Campbell, H. T. Stokes, D. E. Tanner, and D. M. Hatch, ISODISPLACE: A web-based tool for exploring structural distortions, J. Appl. Crystallogr. **39**, 607 (2006).